In Situ Measurements of NiAl Precipitation During Aging of Dual Hardening Hybrid Steels

ORIGINAL RESEARCH ARTICLE

In Situ Measurements of NiAl Precipitation During Aging of Dual Hardening Hybrid Steels

MAGNUS HÖRNQVIST COLLIANDER, STEVE OOI, KRISTINA LINDGREN, TIMO MÜLLER, and MATTIAS THUVANDER

The performance of modern dual hardening steels strongly relies on a well-controlled precipitation processes during manufacturing and heat treatment. Here, the precipitation of intermetallic β-NiAl in recently developed dual hardening steels has been investigated during aging using combined high-energy synchrotron X-ray diffraction and small-angle scattering. The effects of heating rate and aging temperature on the precipitation kinetics and lattice mismatch in two alloys (Hybrid 55 and Hybrid 60) were studied. Precipitation starts already during heating, typically in the temperature range 450 °C to 500 °C. The precipitation process is significantly faster at 570 °C compared to 545 °C for both steel grades, and the number density reaches its maximum already within 1 hours during aging at 545 °C and within 15 minutes during aging at 570 °C. The effect of heating rate is limited, but the precipitation during heating increases in Hybrid 60 when slower heating rate is used. This led to slightly higher volume fractions during subsequent aging, but did not affect the particle size. The lattice mismatch between β-NiAl and the matrix initially develops rapidly with time during aging, presumably due to a developing chemistry of the β phase, until a particle size of around 1.5 nm is reached, whereafter it saturates. After saturation, the lattice mismatch is small, but positive, and independent of temperature during cooling.

https://doi.org/10.1007/s11661-024-07536-z

I. INTRODUCTION

In many demanding applications, such as engines, bearings, or machine tools, exceptional properties in terms of strength, corrosion resistance, and thermal stability are required. Combining these properties is challenging, and consequently many different steels and grades have been developed to meet specific needs. One particular class of materials, denoted dual hardening (DH) steels, has found application in *e.g.*, tooling applications. These materials derive their properties from a combination of coherent intermetallic precipitates for strength and incoherent secondary hardening carbides for improved toughness and ductility.[1,2]

Recently, a new generation of secondary hardening steels, referred to as hybrid steels, has been developed. These combine high-temperature strength (up to 550 °C) from the dual hardening mechanism with high fatigue resistance, high hardenability (dimensional tolerance), weldability, nitriding capability, and improved thermal stability.[3] Low levels of impurities reduce segregation and improves homogeneity and uniformity of the properties, and also enable economic large-batch production. While DH steels have traditionally relied mostly on Mo-rich M_2C carbides[1,2,4] or M_6C,[5] the Cr-rich (but Mo-lean) hybrid steels use Cr-carbides (M_7C_3 or $M_{23}C_6$) as the strengthening phase.[6] The high Cr content also provides corrosion resistance in combination with the high Al content.[7]

It is well known that the precipitation of coherent NiAl in ferritic/martensitic steels is a very rapid process, commencing within a minute of aging (at relevant temperatures), and likely initiating already during heating.[4,8,9] The NiAl particles nucleate homogeneously during annealing in the range 500 °C to 600 °C[10–13] and in turn serve as nucleation sites for the secondary carbides.[2,4,12] This avoids the heterogeneous precipitation of carbides on lath and grain boundaries, and the more homogeneous distribution of secondary carbides greatly improves the toughness.[14]

MAGNUS HÖRNQVIST COLLIANDER, KRISTINA LINDGREN, and MATTIAS THUVANDER are with the Department of Physics, Chalmers University of Technology, 412 96 Gothenburg, Sweden. Contact e-mail: magnus.colliander@chalmers.se STEVE OOI is with the Ovako Corporate R&D, Maxwell Centre, JJ Thompson Avenue, Cambridge CB3 0HE, UK and also with the Ovako Corporate R&D, Building 202, 813 82 Hofors, Sweden. TIMO MÜLLER is with the Deutsches Elektronen-Synchrotron (DESY), 22607 Hamburg, Germany and also with the Anton Paar GmbH, Anton-Paar-Str. 20, 8054 Graz, Austria.
Manuscript submitted February 5, 2024; accepted July 24, 2024.
Article published online August 7, 2024

The NiAl precipitates contain a significant amount of Fe in the initial stages,[2,4,8,15] and the chemistry develops continuously during aging and coarsening.[2,4,15] This in turn affects the lattice mismatch, which is an important parameter for controlling the coarsening rate, and also contributes to the strength through coherency strengthening. A thorough understanding of the NiAl precipitation process is, therefore, essential for optimization of materials and processes.

The present study aims to follow the development of the NiAl precipitates during the entire heat treatment through high-energy synchrotron X-ray scattering. Solution-annealed samples of two different Hybrid steel grades were aged *in situ* at 545 °C and 570 °C, while combined time-resolved small-angle scattering (SAXS) and wide-angle scattering (WAXS) were used to track the microstructure evolution during the different stages. The temperatures were chosen to represent two different scenarios. At 545 °C, peak hardness is reached within 1 hours of aging, and the hardness remains constant for at least 20 hours.[3] At 570 °C, on the other hand, the hardness decreases for aging times longer than somewhere between 1 and 4 hours.

II. EXPERIMENTAL

A. *Material*

Two different hybrid steel grades, designated Hybrid 55 (H55) and Hybrid 60 (H60), were supplied by Ovako AB. The numbers, 55 and 60, refer to the hardness in HRC attainable after tempering, which in turn depends on the difference in carbon content (nominally 0.18 wt pct in H55 and 0.28 wt pct in Hybrid 60). The concentrations of the other alloying elements are very similar in the two grades (see Table I). The materials, in the shape of blocks with dimensions $20 \times 60 \times 60$ mm^3, were solution annealed for 45 minutes at 945 °C (H55) or 1020 °C (H60), followed by air cooling, before the *in situ* aging experiments to comply with the recommended heat treatment procedure.

The microstructure of the as-received material was characterized by scanning electron microscopy (SEM) after standard metallographic preparation (grinding, polishing, and etching with 15 pct Nital). A LEO Ultra 55 SEM operated at 5 keV was used to image the samples in secondary electron mode with the in-lens detector.

B. *In Situ X-ray Scattering*

In situ X-ray scattering experiments were performed at the Swedish Materials Science beamline (P21.2) at the PETRA III synchrotron, DESY, Germany. The photon energy was 60 keV (wavelength $\lambda = 0.2066$ Å) and the beam size on the sample was 0.5×0.5 mm^2. Samples were cut to rods with square cross section, 1×1 mm^2 and length 12 mm. During aging, both WAXS and SAXS data were collected at 10 seconds intervals (acquisition times were 1.5 seconds for WAXS and 5 seconds for SAXS), except for one sample (H55/570/20, see Table II) where data were collected with 20 seconds interval due to an error in the control script. WAXS data were collected in transmission by two VAREX XRD 4343CT flat panel detectors placed approximately 2.8 m downstream of the sample position and offset horizontally to make space for the SAXS flight tube. At the end of the flight tube, approximately 14.5 m from the sample, a Pilatus X CdTe 2M detector was placed for collection of SAXS data. The setup is shown schematically in Figure 1. Exact detector positions were calibrated using LaB_6 (WAXS) and AgBeh (SAXS). All data were reduced to 1D diffractograms using PyFAI 0.20.0.[16,17]

Table I. Chemical Composition in Wt Pct for Hybrid 55 and Hybrid 60

	C	Si	Mn	Cr	Ni	Mo	V	Al
Hybrid 55	0.18	0.1	0.31	5.05	6.10	0.69	0.49	2.30
Hybrid 60	0.28	0.1	0.28	5.61	5.94	0.69	0.49	2.41

The samples were subjected to *in situ* aging in flowing Ar in a Linkam TS-600 furnace. Aging treatments were performed at 545 °C and 570 °C with aging times of 7 and 4 hours, respectively. The heating rate was generally 20 °C min^{-1}, but additional tests with lower heating rate (5 °C min^{-1}) to 570 °C followed by 1 hours aging at the target temperature were also performed. The full set of *in situ* experiments is summarized in Table II. The measured furnace temperature was cross-checked by attaching a thermocouple to a dummy sample during one heating and cooling cycle, showing a maximum deviation of 7 °C between sample and control thermocouple. For the actual tests, the furnace output was used for monitoring and controlling the temperatures. During heating, a constant heating rate was maintained, and no overshoots were observed upon transition to the hold segment (Figure 2(a)). After aging, the samples were cooled as fast as allowed by the furnace, see Figure 2(b) for a typical example. The temperature was below 100 °C within about 6 minutes, and the samples were dismounted once the temperature was below 40 °C to avoid excessive waiting time to reach room temperature.

Automatic Rietveld refinements of the resulting diffractograms from the WAXS detectors proved difficult due to the combination of very small diffraction peaks from the β-NiAl phase and a complex, changing background from the sample environment. Single peak fitting was, therefore, performed using the MATLAB plugin LIPRAS.[18] Refinements were, however, performed for the samples before aging using GSAS-II.[19]

The limited q-range of the SAXS setup resulting from the specific combination of wavelength, beam size, beam stop, and sample-to-detector distance prevented extraction of the Guinier radius (R_g) from the SAXS curves, as determination of q^{-4} background at low q was not possible. Consequently, the average size was determined from the maxima in the Kratky plots, *i.e.*, $R_m = \sqrt{3}/q_m$ where q_m is the position of the maximum in the Iq^2 *vs* q plot.[20,21] R_m is often called the pseudo-Guinier radius, and it has been shown that it is a good estimate of the

Table II. Experimental Parameters for the Different *In Situ* Tests

Sample ID	Material	Heating Rate (°C min^{-1})	Aging Temperature (°C)	Aging Time (h)
H55/545/20	hybrid 55	20	545	7
H55/570/20	hybrid 55	20	570	4
H55/570/5	hybrid 55	5	570	1
H60/545/20	hybrid 60	20	545	7
H60/570/20	hybrid 60	20	570	4
H60/570/5	hybrid 60	5	570	1

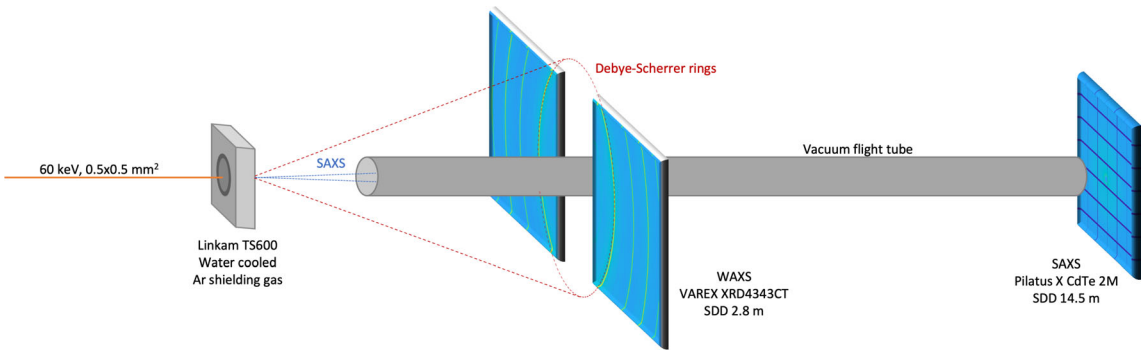

Fig. 1—Schematic of the experimental setup.

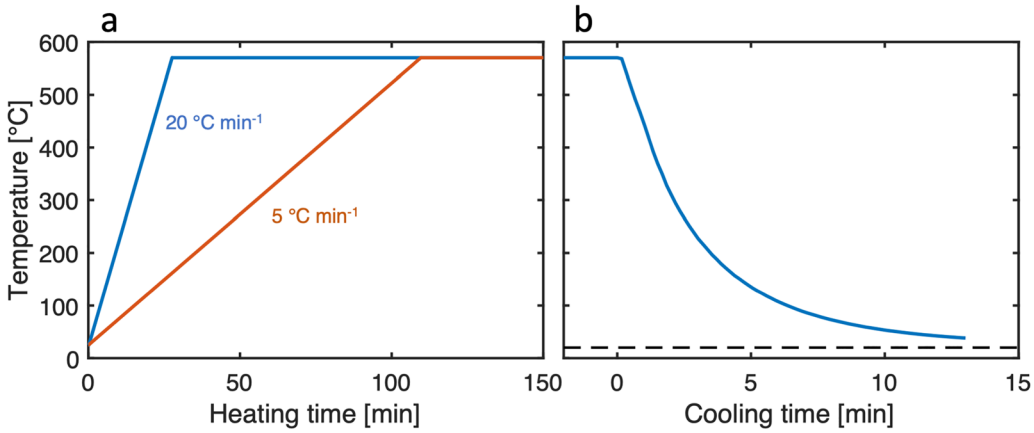

Fig. 2—Typical measured heating/cooling curves to/from 570 °C, exemplified by H60. Both heating rates (20 and 5 °C min^{-1}) are shown in (*a*). Note the constant heating rate and absence of overshoot. The dashed horizontal line in (*b*) indicates 20 °C. The sample was dismounted at a temperature of 40 °C to avoid excessive waiting time.

average particle radius at reasonable levels of polydispersity, *i.e.*, $R_m \approx R$.[22]

Similarly, volume fraction calculations from SAXS signals were prevented by the limited q-range, since the error induced by the required high-q extrapolation to determine the scattering invariant was too large. We, therefore, estimate the volume fraction, V_β, from the intensities of the $(100)_\beta$ and $(200)_{\alpha'}$ diffraction peaks following ASTM E975-13[23] (ignoring the small volume fraction of carbides) as follows:

$$V_\beta = \frac{I^\beta_{100}/R^\beta_{100}}{I^\beta_{100}/R^\beta_{100} + I^{\alpha'}_{200}/R^{\alpha'}_{200}}, \quad [1]$$

where $R^p{}_{hkl}$ is the theoretical intensity of the hkl reflection of phase p, which is given by

$$R^p_{hkl} = \frac{1}{v^2}\left(|F_{hkl}|^2 mLP\right)e^{-2W}, \quad [2]$$

where v is the unit cell volume, F_{hkl} is the structure factor, m is the multiplicity, L is the Lorentz correction, P is the polarization correction, and W is the Debye–Waller factor. We assume a composition of

$(Ni_{0.4}Fe_{0.1})(Al_{0.4}Fe_{0.1})$ for NiAl (based on APT results from References 6, 8, 15, 24 and reported site occupancies[25–27]) and pure Fe for α' when estimating ideal intensities. Polarization correction was applied during data reduction. Lorentz correction for flat panel detectors in transmission from Norby *et al.*[28] was used. Temperature-dependent Debye-Waller factors were calculated from the Debye model (see *e.g.*, Reference 29 for a more detailed description), using the Debye temperatures of 407 K for Fe[30] and 402 K for NiAl.[31] We note that the Debye temperature is temperature dependent, but only weakly so for both transition metals[32–34] and β-NiAl.[35–37] The exact choice of Debye temperature will only affect the absolute magnitude of the calculated volume fractions, and not the relative behavior of the different steels. The approximation clearly introduces a significant uncertainty, but as no experimental values are available for β-NiAl, the error is presumably smaller than using room-temperature values or simply ignoring the temperature effect. However, the uncertainty must be considered when assessing the resulting volume fraction calculations.

As the $(200)_{\alpha'}$ and $(200)_{\beta}$ peaks overlap, we correct the $(200)_{\alpha'}$ intensity by subtracting the intensity of $(200)_{\beta}$, which in turn was calculated from the theoretical intensity ratio between $(200)_{\beta}$ and $(100)_{\beta}$ (as the latter was readily measurable). Consequently, the final equation for the volume fraction is

$$V_{\beta} = \frac{I^{\beta}_{100}/R^{\beta}_{100}}{I^{\beta}_{100}/R^{\beta}_{100} + \left(I_{200} - \left[R^{\beta}_{200}/R^{\beta}_{100}\right] I^{\beta}_{100}\right)/R^{\alpha'}_{200}}. \quad [3]$$

C. *Atom Probe Tomography*

To validate the size and volume fraction measurements from SAXS/WAXS, samples of H55 were placed in a pre-heated furnace and heat treated for 7 hours at 545 °C and 4 hours at 570 °C. From these samples, specimens were prepared using standard electropolishing of 0.3 × 0.3 × 15 mm^3 bars cut by a low-speed diamond saw. A LEAP 3000X HR instrument (Imago Scientific), with a detection efficiency of 37 pct, was used in laser pulsing mode. The laser pulse energy was 0.3 nJ, the temperature was 50 K, the pulse frequency was 200 kHz, and the detection rate was 0.5 pct. The reconstructions were made using the voltage method in the software IVAS 3.6.4 (Cameca) with an image compression factor of 1.65 and a field factor of 4.0.

III. RESULTS AND DISCUSSION

A. *Initial and Final State*

Figure 3 shows SEM images of H55 and H60 in the initial state, where a martensitic structure with retained austenite at martensite lath boundaries can be seen. In H55 (Figure 3(a)) primary MC carbides can be seen, which are absent in H60 (Figure 3(b)) due to the higher solution annealing temperature.

Diffractograms of samples before and after aging are shown in Figures 4(a) and (d). The microstructure of the steels consisted primarily of martensite with a small volume fraction of retained austenite (2.5 and 3.8 vol pct, respectively, for H55 and H60 before aging from the Rietveld refinements). The volume fraction of austenite, qualitatively assessed from the relative intensities of diffraction peaks, had decreased significantly after aging. The austenite peaks in H55 are broad and asymmetric (most clearly seen for the peaks at high diffraction angles), suggesting that small amounts of bainite may have formed.[29] In contrast, the austenite peaks in H60 are narrower and symmetric. There are several changes in peak position, shape, and asymmetry of both the austenite and the martensite peaks, which are issues outside the scope of the present investigation. Here, we note that the agreement in lattice parameters from single peak fitting ($a_{\alpha'}$ = 2.8803 Å and a_{γ} = 3.6043 Å for H55, $a_{\alpha'}$ = 2.8808 Å and a_{γ} = 3.6026 Å for H60) agree well with those from the refinements ($a_{\alpha'}$ = 2.8805 Å and a_{γ} = 3.6081 Å for H55, $a_{\alpha'}$ = 2.8838 Å and a_{γ} = 3.6017 Å for H60), suggesting that the use of single peak fits in the following provides reliable information. Diffraction peaks corresponding to MC carbides are seen in H55 (Figure 4(b)) but not in H60 (Figure 4(e)), confirming the absence of carbides after annealing at 1020 °C.

The $(100)_{\beta}$ peak of NiAl at $2\theta \approx 4$ deg (which was used to track the evolution of β-NiAl during aging) can be clearly observed after aging (see Figures 4(a) and (d) and magnified views in Figures 4(b) and (e)). The peak shape was symmetric and fitted using a single Pearson VII profile. The peaks are narrower after aging at 570 °C, indicating a larger particle size. The presence of β-NiAl precipitates is also visible in the SAXS curves, see Figures 4(c) and (f), and evaluation of q_m indicates final particle radii of around 1.5 and 2.0 nm after aging at 545 °C/7 hours and 570 °C/4 hours, respectively, similar for both alloys.

Apart from the precipitation of NiAl, we also note the presence of many smaller peaks originating from carbides precipitated during aging. The intensities of the carbide peaks were, however, generally too low to allow reliable determination of the particular Cr- rich carbide types. Detailed investigation of the Cr-rich carbide precipitation will require dedicated experiments and will not be further considered here.

B. *Heating*

While the onset of β precipitation could not be resolved in SAXS due to the very small particle size and the limited q-range, it can be monitored *via* the gradual increase in the estimated volume fraction from WAXS, see Figure 5. The intensity starts to increase at temperatures in the range 450 °C to 490 °C. For H55, there is no clear effect of heating rate (Figure 5(a)), whereas H60 shows a more rapid increase in volume fraction with temperature at the slower heating rate (Figure 5(b)). The two alloys respond very similarly during heating at 20 °C min^{-1} (Figure 5(c)), but at 5 °C min^{-1}, the precipitation process appears to start somewhat earlier,

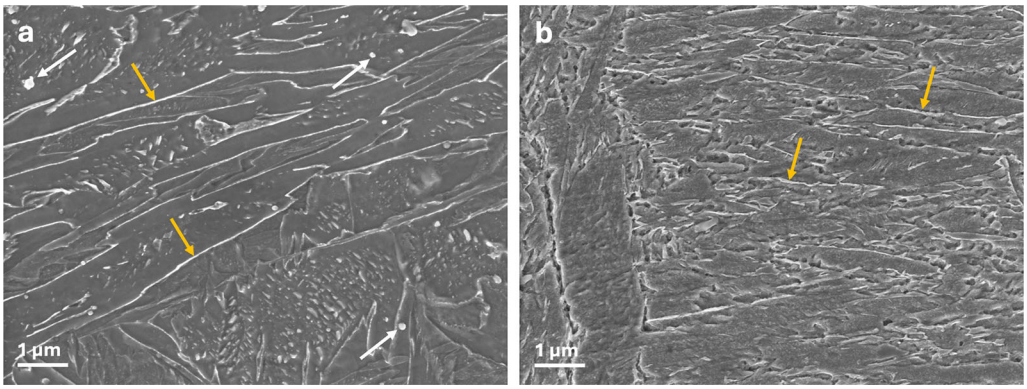

Fig. 3—SEM images showing the fine martensitic structure of (*a*) Hybrid 55, and (*b*) Hybrid 60. The orange arrows mark retained austenite present at the martensite plate boundaries, whereas white arrows indicate undissolved carbides (Color figure online).

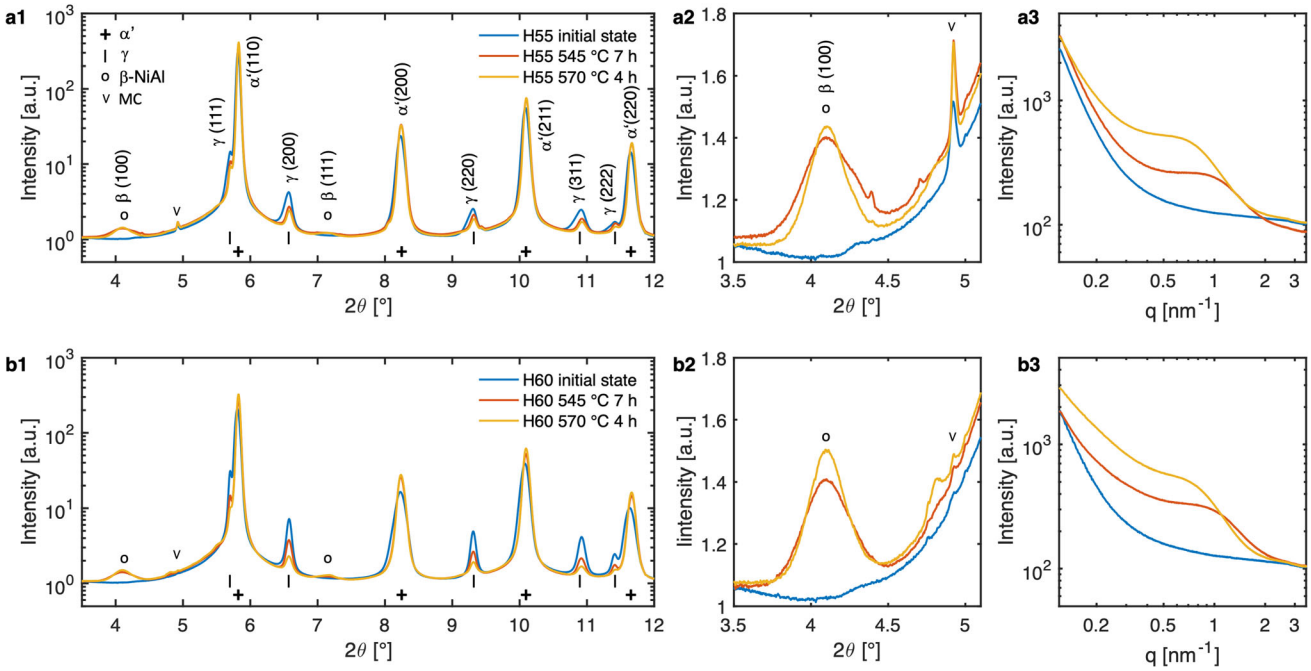

Fig. 4—(*a*) X-ray diffractogram for H55 in the initial stage and after 4 h at 570 °C and 7 h at 545 °C (heating rate 2 + °C min^{-1}); (*b*) Magnified view of the $(100)_\beta$ peak in (a) used for tracking the precipitation of β-NiAl; (*c*) SAXS curves corresponding to the same conditions as in (a). (*d*) to (*f*) are the corresponding figures for H60.

and progress faster, in H60 compared to H55 (Figure 5(d)).

C. *Aging*

Figure 6(a) and (b) shows the evolution of the volume fraction and particle radius (R_g) with time for H55 and H60 aged at 545 °C and 570 °C (heating rate 20 °C min^{-1} in all cases). When the aging temperature is reached, the volume fraction is still very small according to Figure 5 and SAXS data indicate a particles size (radius) in the order of 0.6–0.7 nm. Full saturation (equilibrium volume fractions) does not appear to be fully reached for any of the samples, although the samples aged at 570 °C appear to be closer to saturation after 4 hours than the samples aged at 545 °C aged for 7 hours. The final volume fractions are similar at 545 °C and 570 °C, and slightly higher in H60 compared to H55, although a detailed analysis is difficult considering the significant uncertainty in the volume fraction estimation. The growth rate is considerably slower at 545 °C, where a radius of around 1.5 nm is reached after 7 hours of aging, compared to around 2.0 nm after 4 hours at 570 °C.

The number density evolution, calculated from the average radius and volume fraction,

$$N = \frac{3V_\beta}{4\pi R^3}, \qquad [4]$$

is shown in Figure 6(c). It reaches a maximum after 15–30 minutes (faster at 570 °C) and then decreases continuously. This suggests an early onset of coarsening,

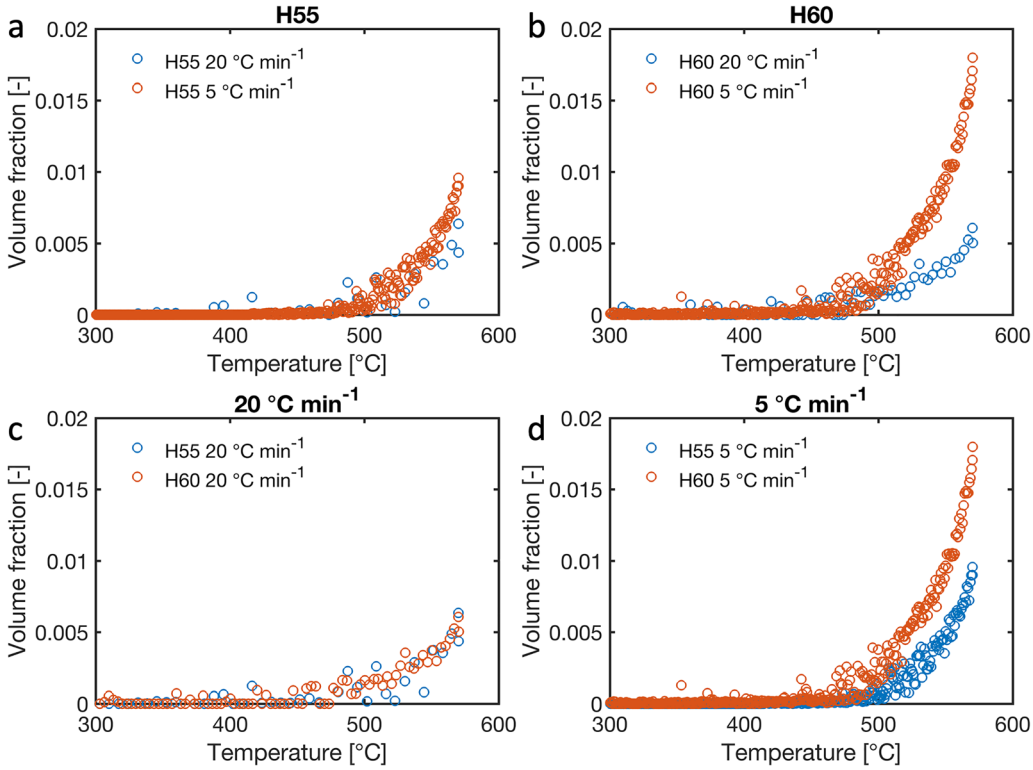

Fig. 5—Evolution of the $(100)_{\beta}$ peak intensity with temperature during heating to 570 °C. (*a*) H55 heated at 20 and 5 °C min^{-1}; (*b*) H60 heated at 20 and 5 °C min^{-1}; (*c*) H55 and H60 heated at 20 °C min^{-1}; (*d*) H55 and H60 heated at 5 °C min^{-1}.

although it is important to remember the caveats associated with the use of q_m for particle size determination, and the fact that this number, even if correct, only represents the average size and does not take the size distribution into account. This is consistent with previous APT measurements in similar alloys, where coarsening of NiAl particles (identified from a decreasing number density) started at very short aging times at temperature between 500 °C and 610 °C,[2,4,15] at the highest temperatures even within minutes.[2,4,15]

The size evolution at long times is well described by a power law:

$$R = kt^n, \qquad [5]$$

where k and n are constants, see Figure 7. The values of the power-law exponent, n, differ slightly between aging temperatures, being higher at 570 °C (n = 0.27) compared to at 545 °C (n = 0.20–0.22), but is virtually independent of alloy. These values are smaller than the value of 1/3 expected when bulk diffusion is the rate-controlling mechanisms.[38–40] However, exponents in this range have been theoretically derived for situations where pipe diffusion along dislocations or low-angle grain boundaries (n = 1/5[41]) or planar diffusion along high-angle grain boundaries (n = 1/4[41–43]) dominates. For NbC precipitation in bcc Fe, it has been shown that the exponent decreases with temperature, from 1/3 at 800 °C to 1/5 at 600 °C, which is suggested to reflect the increased role of diffusion along faults as the temperature (diffusion rate) decreases.[13] The current values of the exponents suggest that the precipitate growth is controlled by diffusion along linear and planar faults. This is consistent with the observations from APT investigations where the precipitates were shown to be aligned on parallel planes, which were suggested to be dislocation arrays.[6] The slightly higher values at 570 °C compared to 545 °C are consistent with previous reports[13] and support the hypothesis that the role of bulk diffusion increases with increasing temperature.

The effect of heating rate on the precipitation process during the subsequent hold time is shown in Figure 8. Consistent with the observation during heating, there is no significant effect on the volume fraction or size evolution in H55. For H60, the volume fraction is consistently higher after heating at 5 °C min^{-1}, in agreement with the faster increase with temperature during heating. The particle size, on the other hand, appears to be unaffected by heating rate. The similar size after heating, independent of heating rate for both steels, indicates that the increased volume fraction during slower heating is primarily related to an increased nucleation rate and not growth of nuclei during heating. This is consistent with the absence of an initial increase in the number density in the H60 sample heated at 5 °C min^{-1}. The higher nucleation rate consumes more of the alloying elements, thereby reducing the driving force and effectively suppressing further nucleation during the hold time. During aging, the increase in radius and volume fraction primarily occurs

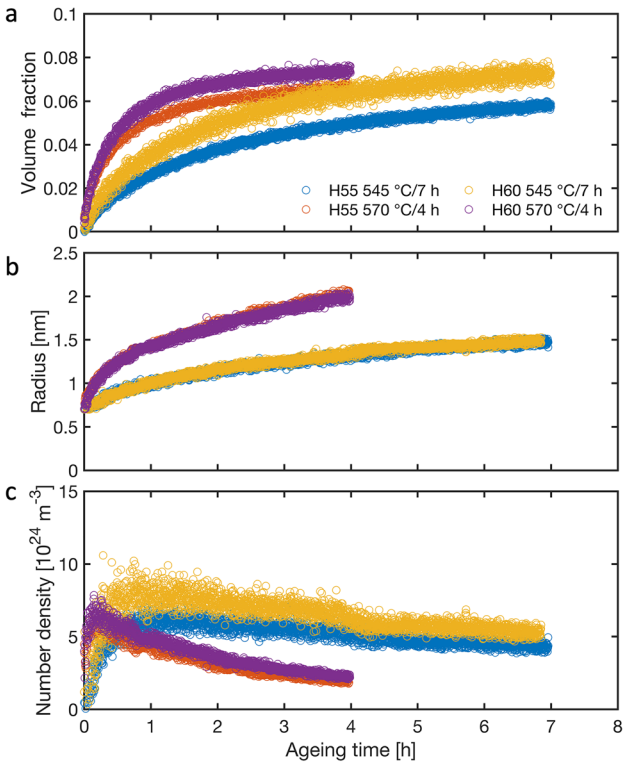

Fig. 6—Evolution of (*a*) volume fraction from the diffraction data, (*b*) average radius from SAXS, and (*c*) calculated number density of β-NiAl in H55 and H60 during aging at 545 °C and 570 °C. The heating rate was 20 °C min^{-1} in all cases.

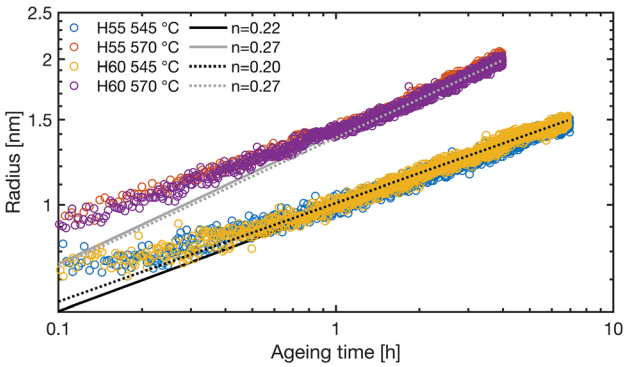

Fig. 7—Fitting of a power law to the evolution of precipitate radius with time during aging after heating at a rate of 20 °C min^{-1}.

through growth of existing particles. Although the coarsening state has not been strictly reached (the volume fraction is still increasing), the decreasing number density suggests that smaller particles are dissolving in favor of growth of larger ones.

The evolution of the lattice parameters of the β and α' phases are shown in Figure 9, together with the resulting constrained lattice mismatch

$$\delta = 2\frac{a_\beta - a_{\alpha'}}{a_\beta + a_{\alpha'}}. \quad [6]$$

The lattice parameter of the β phase is slightly larger than that of the matrix, leading to a positive value of the mismatch. The mismatch decreases with aging time and reaches a value of around 0.45 pct for both alloys during aging at 570 °C. The final mismatch is around 0.55 pct for both alloys after 7 hours aging at 545 °C. These numbers confirm the expected small mismatch leading to a low coarsening rate and good thermal stability. While the coherency strengthening contribution is expected to be small compared to other effects due to the low value of the mismatch, it indicates that for a given particle size, the coherency strengthening effect is larger when aged at lower temperatures.

The decrease in the lattice parameter during aging is much larger for the β phase than for α' (resulting in different scales on the *y*-axis in Figures 9(a) and (b)). Note that δ is the constrained lattice parameter mismatch, which, if heavily influenced by the matrix should be smaller than equilibrium (since $a_{\alpha'}$ is smaller than a_β.), and progressively increases with time as the constraining effects diminish. As the initial value a_β is higher than the value at saturation, the observed development of the lattice parameter is more likely due to an evolving composition. The precipitates can be expected to be richer in Fe in the early stages, due to the abundance of Fe. With time, the in-diffusion of Ni will bring the composition progressively closer to equilibrium. This is consistent with the measured lattice parameters of ~ 2.94 Å for $Fe_{0.6}Al_{0.4}$ at 600 °C,[44] and ~ 2.89 Å for $Ni_{0.6}Al_{0.4}$ at the same temperature calculated from CTE values from Reference 45 combined with the room-temperature lattice parameter from Reference 25. Considering the room-temperature lattice parameter for $Ni_{0.4}Al_{0.4}Fe_{0.2}$ from Reference 25, the expected (unconstrained) lattice parameters at 545 and 570 °C based on the CTEs from Reference 45 are slightly above 2.9 Å, in good agreement with the measurements.

Figure 10 shows that the lattice mismatch develops with size in a very consistent manner, and that it saturates at a radius of around 1.5 nm (which equals around 500 unit cells). As the development of the lattice mismatch is mainly controlled by the lattice parameter of NiAl, which in turn is a function of chemistry, the saturation suggests that the composition of NiAl is relatively close to equilibrium at a particle size of 1.5 nm. Detailed investigations have shown that the chemistry of the β phase continuously develops with time as the particles grow.[2,15] However, the particle sizes in the study by Schober *et al.*[15] were all below a radius of around 1.2 nm (aging was performed at 500 °C for up to 10 hours), smaller than the size where we observe a saturation. Delagne *et al.*[2] performed *ex situ* aging studies at 500 °C, and the particle size was significantly larger (radius 1 nm after 4 hours, 2 nm after 10 hours, and 100 nm after 100 hours). The rate of chemistry change decreased significantly between 4 hours (1 nm) and 10 hours (2 nm), which supports our findings. The fact that the lattice parameters at 570 °C are slightly smaller than at 545 °C, in spite of the higher temperature, could indicate a difference in Fe

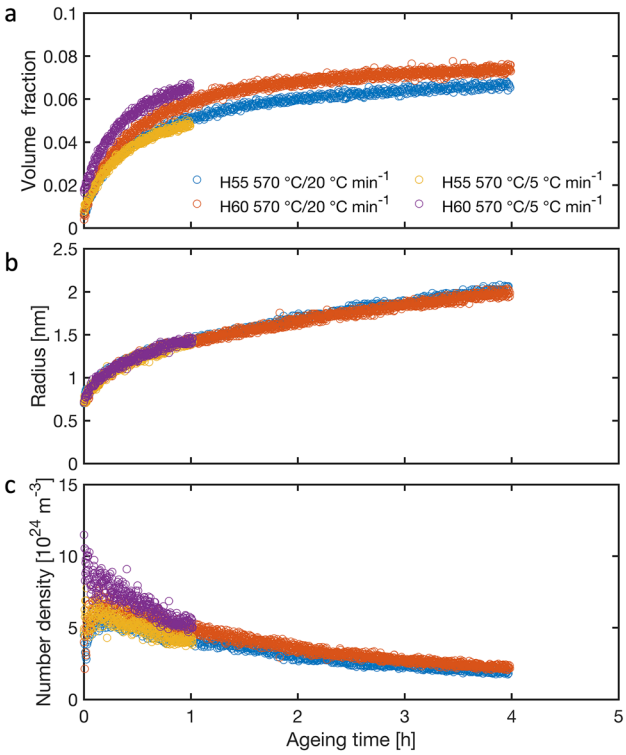

Fig. 8—Evolution of (*a*) volume fraction from the diffraction data, (*b*) average radius from SAXS, and (*c*) calculated number density of β-NiAl in H55 and H60 during aging at 570 °C after heating at 20 °C or 5 °C min^{-1}.

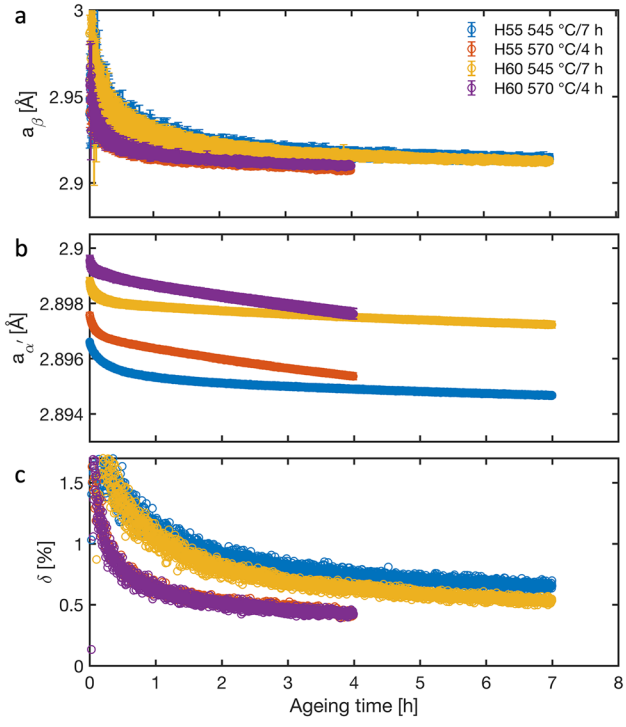

Fig. 9—Evolution of (*a*) β-NiAl lattice parameters, (*b*) martensite lattice parameters, and (*c*) calculated constrained lattice mismatch during the hold time. The heating rate was 20 °C min^{-1} in all cases.

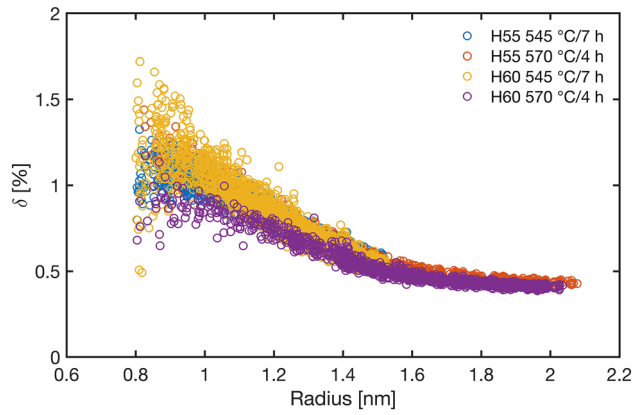

Fig. 10—Evolution of the lattice mismatch with β-NiAl particle size during aging at 545 °C and 570 °C. The heating rate was 20 °C min^{-1} in all cases.

content, but there is also an inherent uncertainty from the single peak fitting.

D. *Cooling*

Finally, we turn our attention to the contraction of β-NiAl during cooling, and the effect on the lattice mismatch. As can be seen in Figures 11(a) and (b), the contraction is similar for α' and β, and the resulting mismatch (Figures 11(c) and (d)) remains approximately constant. The slightly larger mismatch in H55 after aging at 545 °C observed previously remains during cooling. As samples were removed from the furnace before complete cooling, the values of room-temperature lattice parameters and lattice mismatch were calculated by extrapolation of the data in Figures 10(a) and (b) to 20 °C. The results are tabulated in Table III, where the room-temperature lattice parameters of the phases are compared to relevant literature values and found to be consistent. We also note that the martensite lattice parameter is smaller compared to the values obtained from single peak fits before aging, as expected due to the depletion of alloying elements, but it is nevertheless consistent with other reports for martensitic steels, *e.g.*, Villa *et al.*[46]

Next, the coefficients of thermal expansion,

$$CTE = \frac{1}{a}\frac{\partial a}{\partial T} \qquad [7]$$

were considered. The CTEs for the α' and β were obtained by applying Eq. [7] to a second-order polynomial fit of the lattice parameters as a function of temperature in Figures 11(a) and (b). The CTEs agree well with literature values for NiAl[45] and martensite[46] (see Table IV). CTEs for both phases are only weakly temperature dependent, being some 15–20 pct higher at the maximum temperatures compared to room temperature.

There are very few reports of lattice parameters and CTEs for β-NiAl precipitates in precipitation

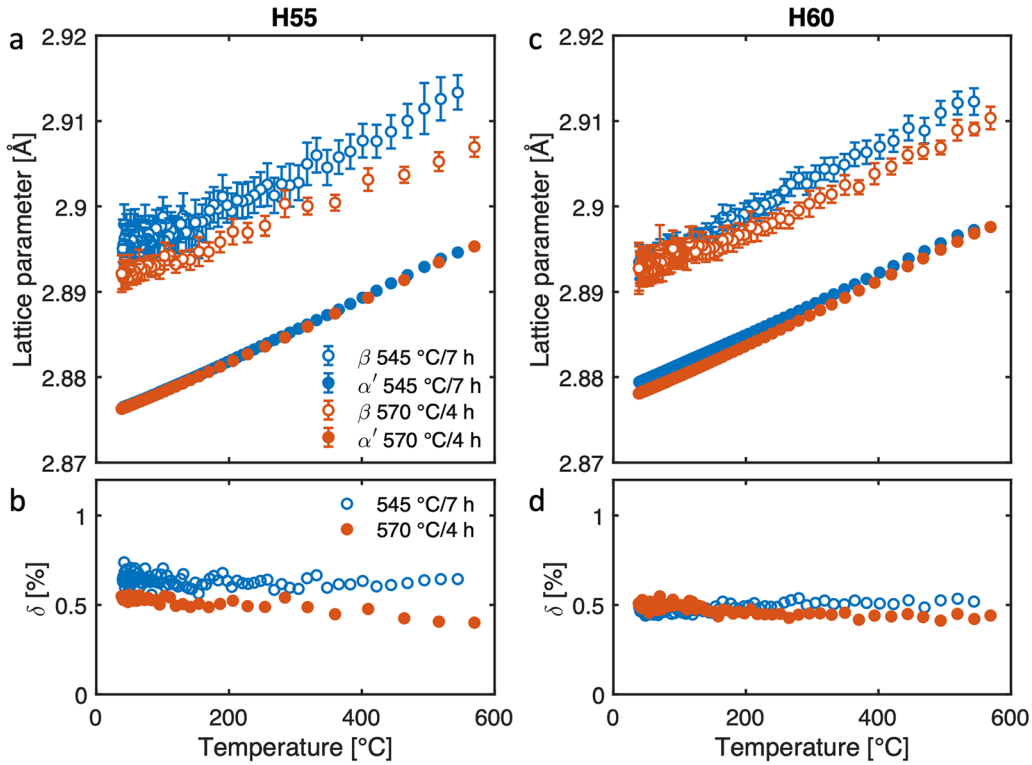

Fig. 11—Evolution of the martensite and β-NiAl lattice parameters in (*a*) H55 and (*b*) H60 with temperature during cooling. (*c*) and (*d*) show the calculated constrained lattice mismatch for H55 and H60, respectively. The heating rate before aging was 20 °C min^{-1} in all cases.

strengthened steels, but Teng *et al.*[47] performed *in situ* neutron diffraction measurements of a Fe−18.9Al–9.8Cr–13Ni–1.8Mo alloy aged at 700 °C for 100 hours, at temperatures up to 600 °C. This alloy had a large volume fraction of β-NiAl, around 27.5 vol pct, with a size of around 100 nm. The lattice parameter of the β phase was smaller than in the present investigation, and the ferrite (rather than martensite) lattice parameter was significantly larger due to the much higher concentrations of alloying elements, the majority of which will expand the lattice. This led to negative values of the lattice mismatch, in contrast to the positive values reported here. CTE_β was obtained from fitting the reported temperature dependence of the lattice parameter using a 1st-order polynomial (rather than a 2nd order as done for the current data, since only four data points were available in Reference 47) and averaging over the entire temperature range. However, we note that a_β increased linearly with temperature from 252 °C, as expected, but the room-temperature value was significantly lower than that obtained by extrapolation of the high-temperature data. Excluding the room-temperature data point, the value of CTE_β is consistent with literature data for pure NiAl, and only slightly larger compared to our results.

E. *Validation and Uncertainties*

Reconstructions of the APT analyses of H55 aged at 545 °C for 7 hours and 570 °C for 4 hours are presented in Figures 12(a, b). The NiAl precipitates and the Cr-rich carbides are highlighted by isoconcentration surfaces, as further described in the figure caption. The former are nearly spherical, and it is clear that the size is larger when tempered at a higher temperature. The carbides are significantly larger and typically plate-like. The Ni:Al ratio is close to 50:50, see Table V, but apart from the presence of minor elements (not shown in the table), the particles also contain large amounts of Fe, around 35-40 at. pct. This is at least partially due to the result of trajectory effects, caused by the difference in evaporation field of the phases. Proxigrams (Figures 12(c, d)) indicate that the Fe content in the center of the particles, where the trajectory effects are smaller, is around 15–20 at. pct. We note that these results are consistent with the literature,[6,8,15,24] as well as our assumed chemistry.

The size and the volume fraction of the NiAl precipitates were determined by applying the parameter-free method by Zhao *et al.*,[49] which uses the radial distribution function (RDF), assuming equally sized precipitates within each analysis and disregarding the depletion around them. Figure 12(e) and (f) shows the Ni–Ni and Al–Al RDFs, which were used to calculate the particle size and volume fractions presented in Table V.

The determined particle radii of 1.1 and 1.5 nm for the two samples are slightly smaller than the 1.5 and 2 nm obtained from the SAXS measurement. The difference could be related to statistical effects (APT probes a very limited volume compared to SAXS, giving a local average), but as the relative differences between

Table III. Extrapolated Room-Temperature Lattice Parameters of Martensite and β-NiAl and Resulting Constrained Lattice Mismatch at Room Temperature Compared to Literature Values

	T (°C)	a_β (Å)	$a_{\alpha'}$ (Å)	δ_{RT} (Pct)
H55 545/7 h	20	2.8931	2.8756	0.60
H55 570/4 h	20	2.8896	2.8757	0.51
H60 545/7 h	20	2.8910	2.8788	0.42
H60 570/4 h	20	2.8901	2.8774	0.44
CIF COD-ID 9008802*	20	2.881	—	—
$Ni_{0.4}Fe_{0.2}Al_{0.4}$[25]	20	2.8879	—	—
$Ni_{0.42}Fe_{0.18}Al_{0.4}$[26]	20	2.8857	—	—
$Ni_{0.5}Al_{0.5}$[48]	20	2.887	—	—
$Ni_{0.5}Al_{0.5}$[45]	20	2.887	—	—
EN 1.4418[46]	25	—	2.875	—
Fe−18.9Al–9.8Cr–13Ni–1.8Mo[47]	27	2.8752	2.8829	− 0.26
Fe−18.9Al–9.8Cr–13Ni–1.8Mo[47]	252	2.8925	2.8945	− 0.07
Fe−18.9Al–9.8Cr–13Ni–1.8Mo[47]	477	2.9003	2.9019	− 0.06
Fe−18.9Al–9.8Cr–13Ni–1.8Mo[47]	600	2.9071	2.9063	0.01

*Value for NiAl from Crystallography Open Database.

Table IV. CTEs of all Phases Obtained During Cooling Compared to Literature Values

	Temperature Range (°C)	CTE_β (10^{-5} K^{-1})	$CTE_{\alpha'}$ (10^{-5} K^{-1})
H55 545/7 h	20–545	1.24	1.20
H55 570/4 h	20–570	1.06	1.18
H60 545/7 h	20–545	1.30	1.23
H60 570/4 h	20–570	1.13	1.23
Average	*20–570*	*1.18 ± 0.11*	*1.21 ± 0.02*
NiAl*[45]	20–570	1.39	—
EN 1.4418[46]	20–475	—	1.3
[Fe−18.9Al–9.8Cr–13Ni–1.8Mo[47]	20–600	1.85	—
Fe−18.9Al–9.8Cr–13Ni–1.8Mo[47]	250–600	1.42	—

Italic values indicate the line containing the average values*The CTEs in Ref. [45] were expressed as polynomials covering the range 20 °C to 1000 °C. The values presented here are the average values in the range 20 °C to 570 °C calculated from the polynomials.

the methods are similar (~35 pct) for both samples, it is more likely that it is a systematic error. Potential sources are differences in temperature between the *in situ* aging and the ex situ heat treatment, as well as effects of polydispersity. For a log-normal size distribution, the approximation $R_m \approx R$ used for size determination from the pseudo-Guinier radius is valid for polydispersity levels around 0.2, and the size will be increasingly overestimated when the width of the size distribution increases.[22] To estimate the level of polydispersity in our data, we extracted the size of all individual particles in the analyzed volumes using isosurfaces. While iso-surface-based size determination is not expected to be quantitatively correct, it allows the width of the particle size distribution to be estimated. Figure 13 shows histograms of the particle sizes in the two specimens, and the result of fitting a log-normal distribution. The polydispersity parameter in both cases is around 0.35, which according to the analysis in Reference 22 corresponds to an overestimation of the radius by around 30 pct using the pseudo-Guinier radius. Considering this, the results of APT and SAXS are in good agreement, but it suggests that the sizes from the SAXS measurements presented are overestimations of the real average particle size. However, assuming similar levels of polydispersity in H55 and H60, this does not affect the conclusions drawn in the present study. While it would be possible to perform first-order corrections to the particle sizes derived from SAXS based on this, such corrections would assume a constant polydispersity during aging, which is unlikely to be true based on current knowledge of the precipitation process in metallic materials, in particular in the coarsening stage. The accuracy of the correction is, therefore, not known and would introduce more uncertainties into the analysis.

The volume fractions given by RDF methods are around 7.3 vol pct for both heat treatment conditions, which is consistent with the results obtained from WAXS (6–7 vol pct). The APT values are, however, not corrected for the presence of Fe in the particles, which would increase the volume fraction linearly with the assumed Fe concentration. This would result in higher volume fractions from APT compared to WAXS, which could, again, be related to possible differences in temperature of the *in situ* and *ex situ* heat treatments, but also the initial heating rate, which can have a significant effect on the volume fraction (but not on the

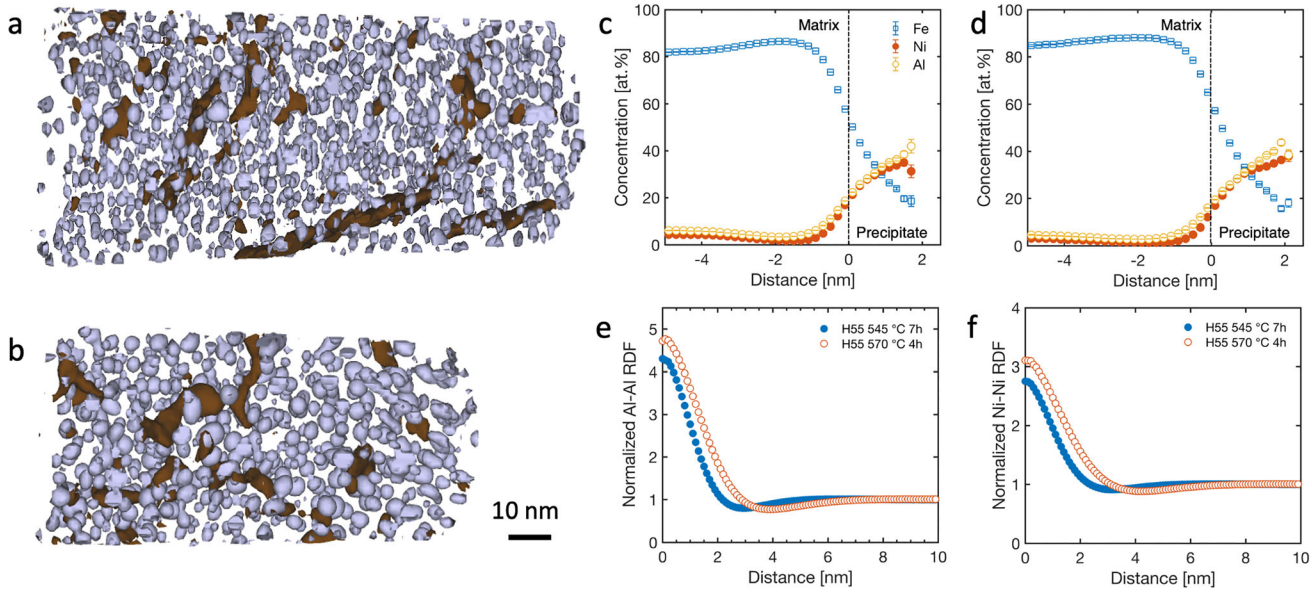

Fig. 12—APT reconstructions showing NiAl precipitates (purple) and Cr-rich carbides (brown) in the aged Hybrid 55 samples aged at (*a*) 545 °C for 7 h; and (*b*) 570 °C for 4 h. (a) NiAl isosurfaces were created using Ni + Al = 25 pct and (b) Ni + Al = 23 pct. The different levels were selected to provide best visual agreement when comparing the isosurfaces and the atom maps. In both cases the carbide isosurfaces were created using Cr + C = 15 pct. Proxigrams of Fe, Ni, and Al are shown for (*c*) H55 545 °C 7 h and (*d*) H55 570 °C 4 h. (*e*) and (*f*) show the normalized Al–Al and Ni–Ni RDFs, respectively.

Table V. Characteristics of the NiAl Precipitates in Hybrid 55, from APT

Sample	Average Radius (nm)	Volume Fraction (Pct)	Ni	Al	Fe	Ni/(Ni + Al)
RDF 545 °C/7 h	1.1	7.3	30.1 (1)	28.9 (1)	35.7 (1)	0.51
RDF 570 °C/4 h	1.5	7.3	28.5 (1)	27.6 (1)	39.2 (1)	0.49

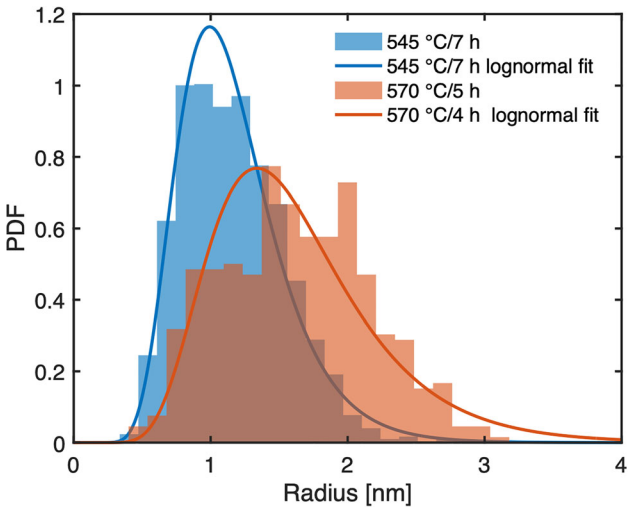

Fig. 13—Histograms of the particle sizes estimated using a Ni + Al isoconcentration of 25 at. pct. The lines show the results of fitting a log-normal distribution function to the experimental data. Note that the polydispersity parameter from the log-normal distribution is approximately the same for both samples, despite the wider distribution on a linear scale.

particle size), see Figure 8. Comparison between the techniques is not straightforward, the volume fractions from both APT and WAXS depend on the assumed chemistry of the particles. In the case of APT, the volume fraction varies linearly with the assumed Fe concentration, as mentioned, whereas in WAXS, the effect is more intricate as the structure factors used for calculation of ideal intensities depend not only on the assumed composition of the particles (Fe content), but also on the site occupancy. In general, however, an increased Fe concentration will lead to an increase in the estimated volume fraction. The fact that the chemistry is expected to change during the precipitation process, from very Fe rich in the early stages to lower concentrations at longer times,[6,8,15,24] means that the structure factors will vary during the experiment, which we cannot account for in the present investigation. However, assuming a similar evolution of precipitate chemistry in H55 and H60, and a negligible dependence on temperature as the differences between the aging temperatures is relatively small, the conclusions drawn here are not affected.

The number density is calculated from the radius and volume fraction, and the uncertainty consequently depends on the accuracy in the determination of both these quantities. The effects are, therefore, more difficult

to discuss, in particular with respect to the effects of changing chemistry on the volume fractions. However, under the assumptions above, the overall behavior and the relative differences between the different samples will not change.

In summary, given the uncertainties in both size and volume fraction discussed above, the results presented in this study should be considered as qualitative rather than quantitative. Nevertheless, the relative differences between samples are considered correct, providing insights into the effect of different heat treatment temperatures, heating rates and alloy chemistry on the precipitation process. We note that an accurate time-resolved analysis of both size and volume fraction during aging would be enabled by SAXS measurement with a better tuned setup with a q-range allowing model-dependent fitting of the data. If such experiments are performed in anomalous scattering mode (ASAXS), information about the time-dependent particle chemistry could be simultaneously obtained.

IV. CONCLUSIONS

Using *in situ* high-energy X-ray diffraction and SAXS, we have investigated the development of β-NiAl precipitates in two DH steels (H55 and H60) through the entire aging treatment. We observe that

- Precipitation starts during heating, typically in the temperature range 450 °C to 500 °C. The precipitation during heating is more sensitive to heating rate for H60 compared to H55.
- The precipitation process (both in terms of volume fraction and particle size) is significantly faster at 570 °C compared to 545 °C.
- The volume fractions in H60 are slightly higher than in H55 when aged at the same temperature, while the particles size does not differ between different alloys aged at the same temperature.
- The number density peaks within 1 hours during aging at 545 °C and within 15 minutes during aging at 570 °C, and subsequently undergoes a continuous decrease.
- There is no pronounced effect of heating rate on the precipitation process in H55 during the subsequent hold time. H60, on the other hand, shows a slightly higher volume fraction, but the same particle size, after heating at a lower rate.
- The lattice mismatch between NiAl and the matrix initially develops rapidly with time, presumably due to a developing chemistry of the β phase, until a particle size (radius) of around 1.5 nm is reached, whereafter it saturates. This suggests that the rate of chemistry change has slowed down significantly at this size. After saturation, the lattice mismatch is small, but positive, and independent of temperature during cooling.

ACKNOWLEDGMENTS

We acknowledge DESY (Hamburg, Germany), a member of the Helmholtz Association HGF, for the provision of experimental facilities. Parts of this research were carried out at PETRA III, beamline P21.2. Beamtime was allocated for proposal I-20190135 EC. The work was in part performed at Chalmers Materials Analysis Laboratory (CMAL).

FUNDING

Open access funding provided by Chalmers University of Technology.

CONFLICT OF INTEREST

Steve Ooi is an employee of Ovako, the supplier of the alloys used in this study.

REFERENCES

1. R. Hamano: *Metall. Trans. A*, 1993, vol. 24, pp. 127–39. https://doi.org/10.1007/BF02669610.
2. D. Delagnes, F. Pettinari-Sturmel, M.H. Mathon, R. Danoix, F. Danoix, C. Bellot, P. Lamesle, and A. Grellier: *Acta Mater.*, 2012, vol. 60, pp. 5877–88. https://doi.org/10.1016/j.actamat.2012.07.030.
3. J.E. Andersson, F. Lindberg, and S. Ooi: *ASTM Spec. Techn. Publ.*, 2020, vol. 1623, pp. 436–54. https://doi.org/10.1520/STP162320190163.
4. S.D. Erlach, H. Leitner, M. Bischof, H. Clemens, F. Danoix, D. Lemarchand, and I. Siller: *Mater. Sci. Eng. A*, 2006, vol. 429, pp. 96–106. https://doi.org/10.1016/j.msea.2006.05.071.
5. M. Hofinger, M. Staudacher, M. Ognianov, C. Turk, H. Leitner, and R. Schnitzer: *Micron*, 2019, vol. 120, pp. 48–56. https://doi.org/10.1016/j.micron.2019.02.004.
6. S. Jakob, M. Hörnqvist Colliander, J. Kawser, S. Rashidi, S.W. Ooi, and M. Thuvander: *Metall. Mater. Trans. A*, 2024, vol. 55A, pp. 870–79.
7. C. Örnek, B. Payam, A. Gloskovskii, K. Kazmanlı, N. Mohamed, B. Derin, M. Ürgen, C.E. Chou, H.W. Yen, B. Avcı, and S. Ooi:

Npj Mater. Degrad., 2023, vol. 7, p. 71. https://doi.org/10.1038/s41529-023-00392-z.
8. S. Erlach, F. Danoix, H. Leitner, P. Auger, I. Siller, and H. Clemens: *Surf. Interface Anal.*, 2007, vol. 39, pp. 213–20. https://doi.org/10.1002/sia.2517.
9. H. Leitner, M. Bischof, H. Clemens, S. Erlach, B. Sonderegger, E. Kozeschnik, J. Svoboda, and F.D. Fischer: *Adv. Eng. Mater.*, 2006, vol. 8, pp. 1066–77. https://doi.org/10.1002/adem.200600165.
10. V. Seetharaman, M. Sundararaman, and R. Krishnan: *Mater. Sci. Eng.*, 1981, vol. 47, pp. 1–11. https://doi.org/10.1016/0025-5416(81)90034-3.
11. D.H. Ping, M. Ohnuma, Y. Hirakawa, Y. Kadoya, and K. Hono: *Mater. Sci. Eng. A*, 2005, vol. 394, pp. 285–95. https://doi.org/10.1016/j.msea.2004.12.002.
12. F. Danoix, R. Danoix, J. Akre, A. Grellier, and D. Delagnes: *J. Microsc.*, 2011, vol. 244, pp. 305–10. https://doi.org/10.1111/j.1365-2818.2011.03537.x.
13. M. Perrut, M.H. Mathon, and D. Delagnes: *J. Mater. Sci.*, 2012, vol. 47, pp. 1920–29. https://doi.org/10.1007/s10853-011-5982-x.
14. C. Bellot, P. Lamesle, and D. Delagnes: *Acta Metall. Sin.*, 2013, vol. 26, pp. 553–57. https://doi.org/10.1007/s40195-013-0078-z.
15. M. Schober, R. Schnitzer, and H. Leitner: *Ultramicroscopy*, 2009, vol. 109, pp. 553–62. https://doi.org/10.1016/j.ultramic.2008.10.016.
16. G. Ashiotis, A. Deschildre, Z. Nawaz, J.P. Wright, D. Karkoulis, F.E. Picca, and J. Kieffer: *J. Appl. Crystallogr.*, 2015, vol. 48, pp. 510–19. https://doi.org/10.1107/S1600576715004306.
17. J. Kieffer, V. Valls, N. Blanc, and C. Hennig: *J. Synchrotron Radiat.*, 2020, vol. 27, pp. 558–66. https://doi.org/10.1107/S1600577520000776.
18. G. Esteves, K. Ramos, C.M. Fancher, J.L. Jones: LIPRAS: Line-Profile Analysis Software. (2017). https://doi.org/10.13140/RG.2.2.29970.25282/3.
19. B.H. Toby and R.B. Von Dreele: *J. Appl. Crystallogr.*, 2013, vol. 46, pp. 544–49. https://doi.org/10.1107/S0021889813003531.
20. F. De Geuser and A. Deschamps: *C. R. Phys.*, 2012, vol. 13, pp. 246–56. https://doi.org/10.1016/j.crhy.2011.12.008.
21. A. Deschamps and F. De Geuser: *Metall. Mater. Trans. A*, 2013, vol. 44A, pp. 77–86. https://doi.org/10.1007/s11661-012-1435-7.
22. A. Deschamps and F. De Geuser: *J. Appl. Crystallogr.*, 2011, vol. 44, pp. 343–52. https://doi.org/10.1107/S0021889811003049.
23. A. International: *Astm*, 2003, https://doi.org/10.1520/E0975-13.necessary.
24. S. Erlach, I. Siller, H. Leitner, and H. Clemens: *Int. J. Microstruct. Mater. Prop.*, 2008, vol. 3, pp. 373–82. https://doi.org/10.1504/IJMMP.2008.018741.
25. R. Hu, H.N. Su, and P. Nash: *Pure Appl. Chem.*, 2007, vol. 79, pp. 1653–73. https://doi.org/10.1351/pac200779101653.
26. L.M. Pike, I.M. Anderson, C.T. Liu, and Y.A. Chang: *Acta Mater.*, 2002, vol. 50, pp. 3859–79. https://doi.org/10.1016/S1359-6454(02)00192-1.
27. I.M. Anderson, A.J. Duncan, and J. Bentley: *Intermetallics*, 1999, vol. 7, pp. 1017–24. https://doi.org/10.1016/S0966-9795(99)00013-8.
28. P. Norby: *J. Appl. Crystallogr.*, 1997, vol. 30, pp. 21–30. https://doi.org/10.1107/S0021889896009995.
29. H.J. Stone, M.J. Peet, H.K.D.H. Bhadeshia, P.J. Withers, S.S. Babu, and E.D. Specht: *Proc. R. Soc. A*, 2008, vol. 464, pp. 1009–27. https://doi.org/10.1098/rspa.2007.0201.
30. T. Paakkari: *Acta Crystallogr. Sect. A*, 1974, vol. 30, pp. 83–86. https://doi.org/10.1107/S0567739474000131.
31. A.G. Fox: *J. Phys. F*, 1983, vol. 13, pp. 1593–1605. https://doi.org/10.1088/0305-4608/13/8/007.
32. J. Prakash, L. Pathak, and M. Hemkar: *Aust. J. Phys.*, 1975, vol. 28, p. 63. https://doi.org/10.1071/PH750063.
33. D.R. Chipman: *J. Appl. Phys.*, 1960, vol. 31, pp. 2012–15. https://doi.org/10.1063/1.1735487.
34. E.A. Owen and R.W. Williams: *Nature*, 1938, vol. 142, p. 915. https://doi.org/10.1038/142915a0.
35. H.X. Cao and L.M. Peng: *Acta Crystallogr. A*, 1999, vol. 55, pp. 926–32. https://doi.org/10.1107/s0108767399005176.
36. Y. Lozovoi and Y. Mishin: *Phys. Rev. B*, 2003, vol. 68, pp. 1–10. https://doi.org/10.1103/PhysRevB.68.184113.
37. Z. Wen, Y. Zhao, H. Hou, J. Tian, and P. Han: *Superlatt. Microstruct.*, 2017, vol. 103, pp. 9–18. https://doi.org/10.1016/j.spmi.2017.01.010.
38. C. Wagner: *Berichte Der Bunsengesellschaft Für Physikalische Chemie*, 1961, vol. 65, pp. 581–91.
39. I.M. Lifshitz and V.V. Slyozov: *J. Phys. Chem. Solids*, 1961, vol. 19, pp. 35–50. https://doi.org/10.1016/0022-3697(61)90054-3.
40. J.A. Marqusee and J. Ross: *J. Chem. Phys.*, 1983, vol. 79, pp. 373–78. https://doi.org/10.1063/1.445532.
41. A.J. Ardell: *Acta Metall.*, 1972, vol. 20, pp. 601–09. https://doi.org/10.1016/0001-6160(72)90015-6.
42. J.J. Hoyt: *Acta Metall. Mater.*, 1991, vol. 39, pp. 2091–98. https://doi.org/10.1016/0956-7151(91)90179-5.
43. M.V. Speight: *Acta Metall.*, 1968, vol. 16, pp. 133–35. https://doi.org/10.1016/0001-6160(68)90081-3.
44. M. Zhao, K. Yoshimi, K. Maruyama, and K. Yubuta: *Acta Mater.*, 2014, vol. 64, pp. 382–90. https://doi.org/10.1016/j.actamat.2013.10.051.
45. R.D. Noebe, R.R. Bowman, and M.V. Nathal: *Int. Mater. Rev.*, 1993, vol. 38, pp. 193–232. https://doi.org/10.1179/imr.1993.38.4.193.
46. M. Villa, F. Niessen, and M.A.J. Somers: *Metall. Mater. Trans. A*, 2018, vol. 49A, pp. 28–40. https://doi.org/10.1007/s11661-017-4387-0.
47. Z.K. Teng, G. Ghosh, M.K. Miller, S. Huang, B. Clausen, D.W. Brown, and P.K. Liaw: *Acta Mater.*, 2012, vol. 60, pp. 5362–69. https://doi.org/10.1016/j.actamat.2012.05.033.
48. H.N. Su and P. Nash: *J. Alloys Compd.*, 2005, vol. 403, pp. 217–22. https://doi.org/10.1016/j.jallcom.2005.05.032.
49. H. Zhao, B. Gault, D. Ponge, D. Raabe, and F. De Geuser: *Scr. Mater.*, 2018, vol. 154, pp. 106–10. https://doi.org/10.1016/j.scriptamat.2018.05.024.